Experiments in Fluids 35 (2003) 49–57
DOI 10.1007/s00348-003-0634-9

Intensity broadening of internally reflected laser beam from a meniscus formed in a capillary pore—applied for automated liquid column height measurements

K.D. Kihm, D.M. Pratt

Abstract An automated liquid column height measurement technique using the total internal reflection of a collimated laser beam from the convex meniscus surface is proposed. This new technique can alleviate the shortcomings of the traditional cathetometer that tends to introduce user bias. Experimental measurements and theoretical predictions have been conducted to examine the detected signal broadening and measurement uncertainties of the proposed technique, resulting from (1) the finite laser-beam diameter, (2) the capillary pore diameter, (3) the beam steering by thermal gradients, and (4) the beam steering by density variations of the liquid inside a capillary pore. For the collimated 52.6-μm diameter laser beam, for three different tested pores of 0.5, 1.0, and 2.0 mm diameter, the overall uncertainty of the wicking height measurement is estimated to be ±12 μm in the case of on-axis detection, and ±24 μm in the case of off-axis detection.

1 Introduction

Dynamic wetting characteristics result from non-isothermal liquid–vapor interfacial temperatures near the contact line arising from both non-uniform substrate wall temperatures and non-uniform evaporation (Pratt and Kihm 2003). Since for most liquids surface tension decreases with increasing temperature, a surface tension gradient is established in adverse to the temperature gradient. These surface tension gradients induce thermocapillary stresses pulling down the contact line, which can degrade the wettability of evaporating liquid (Hocking 1995). Ehrhard and Davis (1991) showed retardation in thin-film spreading or wetting caused by thermocapillary stresses. Recent studies of rewetting of various configurations (Sen and Davis 1982; Anderson and Davis 1994; Ha and Peterson 1994; Chan and Zhang 1994; Pratt and Hallinan 1997) show that the measured maximum wicking heights are lower than the predictions obtained from the typical Laplace–Young equation, by as much as 30%.

The degradation of wetting will lead to a reduction in the capillary pumping potential in capillary heat-transfer devices and thus a reduction in the ability to transport energy. Reliable wicking height measurements are crucial to create a fully validated physical model describing the wetting characteristics associated with thermocapillary. An accurate, repeatable, user-independent device is needed to determine the wicking heights or their differentials. A cathetometer, essentially consisting of a telescope with a horizontal hairline to be visually matched with the meniscus bottom, has been traditionally used to measure the capillary height but with relatively large uncertainties of up to ±50 μm. This occurs because of the subjective judgment of the hairline matching by individual researchers.

A laser-scanning concept using the total internal reflection from the meniscus surface is examined as a new wicking height measurement tool that provides accuracy and repeatability thus, eliminating user bias. Discussions are presented on various broadening factors for detected signals of the reflected laser-beam intensity and for their effects on the detection accuracy for wicking heights.

2 Experimental setup

The idea of a laser-scanning technique is based on the total internal reflection of a collimated laser beam from the meniscus bottom point (Fig. 1). When the incident angle θ_i exceeds the critical angle θ_c, the light ray will be totally reflected internally. From Snell's law (Hecht 2002), the critical angle, which is equivalent to the limiting case of θ_t=90°, is given as

$$\theta_c = \sin^{-1}(n_t/n_i) \quad (1)$$

where n_t and n_i represent the refractive index of the transmitting medium (external gas or vapor above the meniscus) and incident medium (internal or liquid in the pore), respectively.

Received: 4 November 2002 / Accepted: 2 April 2003
Published online: 18 June 2003

K.D. Kihm (✉)
Department of Mechanical Engineering,
Texas A&M University, College Station, TX 77843, USA
E-mail: ken-kihm@tamu.edu
Tel.: +1-979-8452143
Fax: +1-979-8622418

D.M. Pratt
AFRL/VAS, Wright–Patterson Air Force Base,
Dayton, OH 45433, USA

This material is based on work partially supported by the National Research Council–Summer Faculty Fellow Program (SFFP) for Dr K. D. Kihm and partially supported by the Air Force Office of Scientific Research Laboratory Research Initiation Request, granted to both authors. Any opinions, findings, and conclusions or recommendations expressed in this publication are those of the authors and do not necessarily reflect the views of the NRC or the AFOSR.

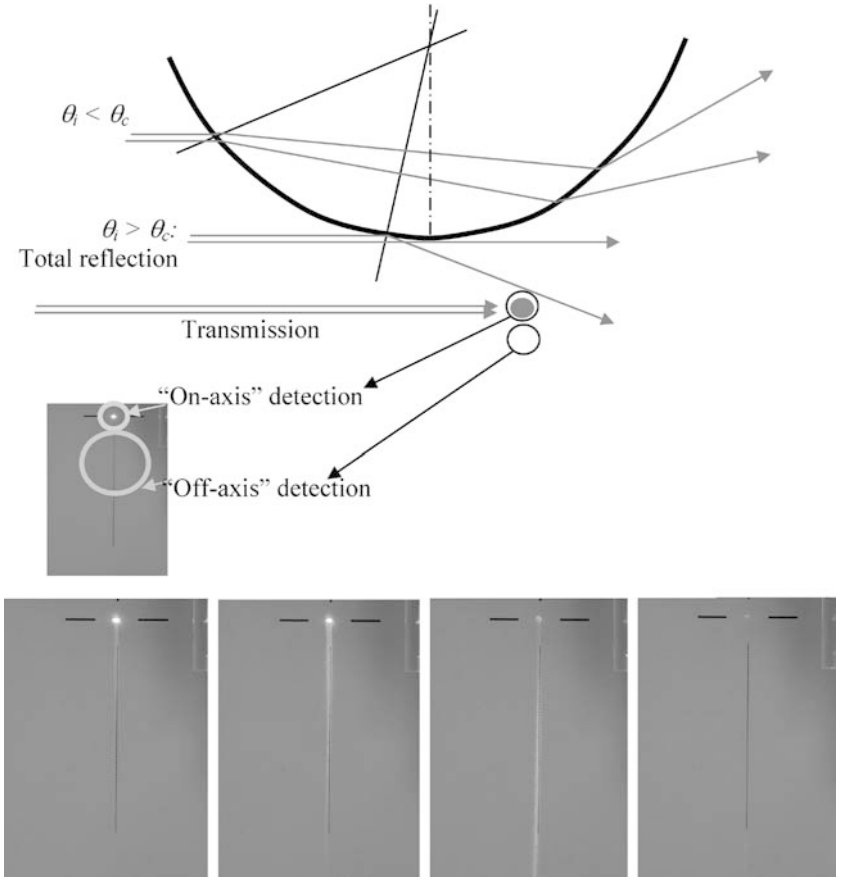

Fig. 1. Illustration of the wicking height detection principle by laser scanning, based on the total internal reflection from the meniscus bottom

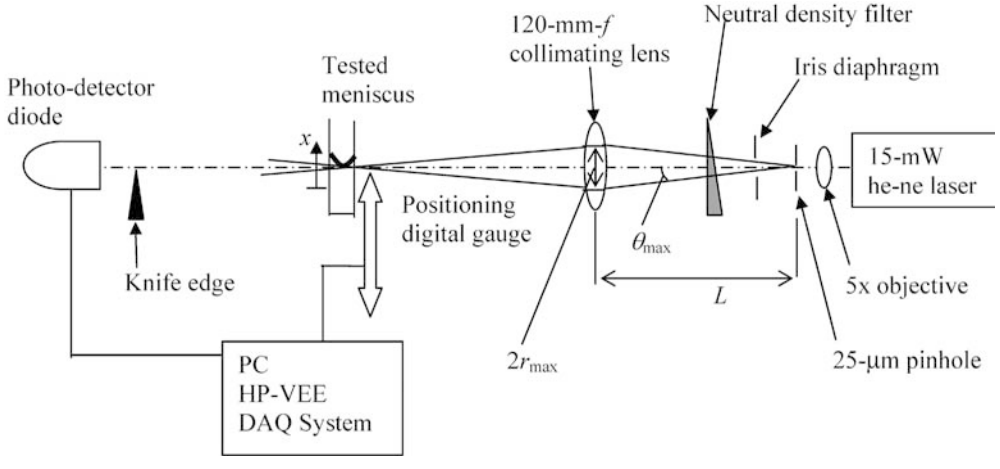

Fig. 2. Experimental setup of the wicking height measurement technique by laser scanning

The paired arrows in Fig. 1 schematically represent the collimated laser beam of a finite diameter, which is scanned in the upward direction. Until it reaches the bottom of the meniscus, the laser beam will be mostly transmitted through the optically transparent liquid and glass pore. When the top of the beam reaches the meniscus bottom, a small portion of the beam will be deflected by the total internal reflection. The portion of the totally reflected beam will increase with the beam advancement causing the size and intensity of the projected image of the reflected beam to increase, as shown in the inset photographs. Thus, the off-axis detection, which is regarded as the detector location below the optic axis, will record image intensity that will increase from zero to a maximum value and then decrease to zero as the laser beam passes the meniscus bottom. The transmission intensity, on the other hand, will continually decrease, to zero eventually, when the entire beam is totally reflected. Thus, the on-axis recorded intensity will monotonically decrease to zero, transitioning from the entire transmission to the entire reflection with laser-beam advancement.

The experimental setup of the laser-scanning technique is schematically illustrated in Fig. 2. An approximately 1.1-mm diameter beam emitted from a linearly polarized 15-mW helium–neon laser is collimated onto the 25-μm diameter pinhole aperture to spatially filter the "tail" noise

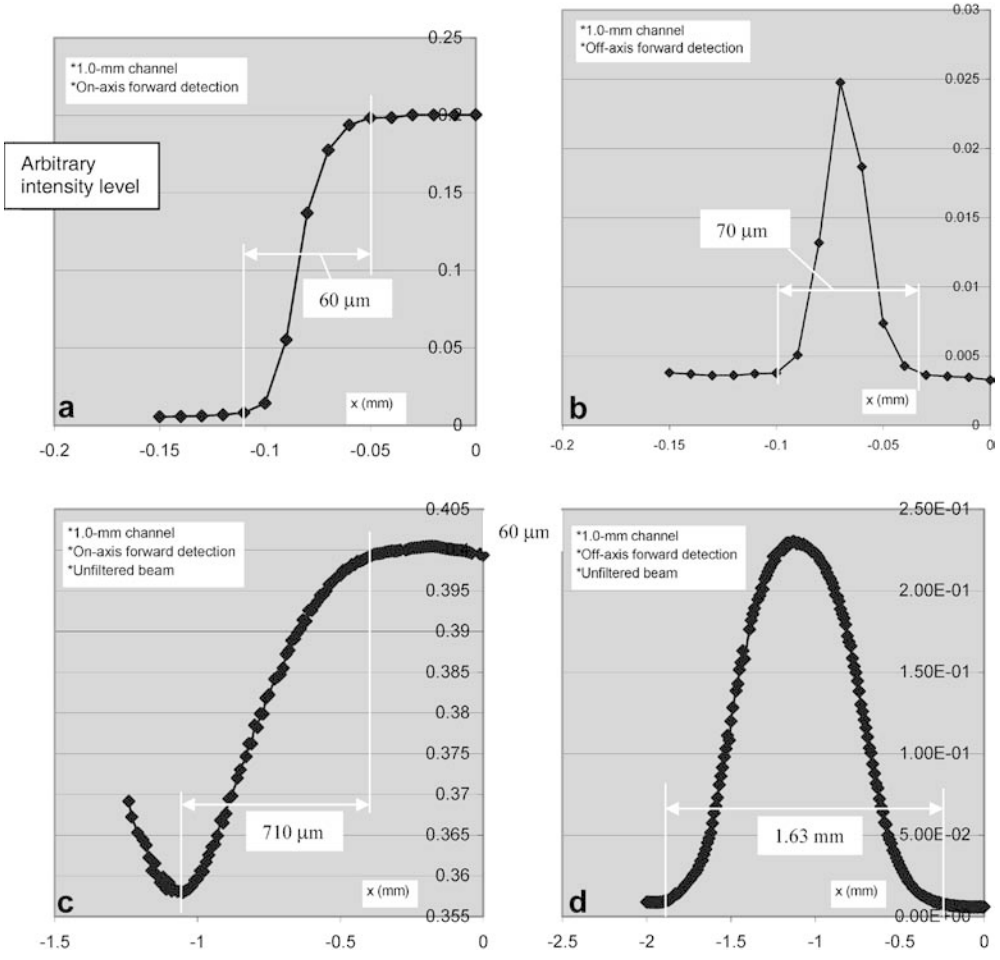

Fig. 3a–d. Dependence of the signal broadening on the beam diameter for 1.0-mm wide channel. For collimated 52.6 μm diameter beam, **a** 60 μm (on-axis detection) and **b** 70 μm (off-axis detection); for uncollimated 1.1-mm diameter beam, **c** 710 μm (on-axis detection) and **d** 1.63 mm (off-axis detection)

of the Gaussian beam. The pinhole inevitably produces Fraunhofer diffraction-ring patterns that increase the unwanted signal noise level and the iris diaphragm is effectively used to spatially block the second or higher order diffraction rings. The neutral density filter limits the necessary laser power for image detection/discrimination in order to minimize the possible laser heating of the working fluid inside the capillary pore.

The diverging laser beam from the pinhole is collimated into the test section using a bi-convex lens of f=120-mm at a unit (×1) magnification. The knife edge helps to narrowly specify the detection angle for the on-axis detection. For the case of off-axis detection, the knife edge is inverted vertically to cut off the transmitted portion of the laser beam. The voltage output from the photo-detector diode unit, which is linearly proportional to the detected image intensity, is then sent to a PC platform for data processing. The tested capillary pore is placed on a precise positioning system and its digital output at 5-μm reading resolution, indicating its relative height to a fixed zero point, is sent to the PC in a synchronized way with the photo-detector output.

3
Signal broadening and measurement uncertainties

Under absolutely free from non-ideal factors including zero beam diameter with no diffraction from the meniscus, a perfect lens with no spherical aberration, and no beam steering by temperature or concentration gradients, the on-axis signal should be a perfect step change at the instant of contact and the off-axis detection must show a "spike" line shape. However, those non-ideal factors contribute to broadening the ideal step change into a gradually changing signal, and the ideal spike-like signal into Gaussian distribution.

3.1
Effect of a finite beam diameter

When the top end of the beam touches the center of the meniscus (Fig. 1), the beam deflection is incurred by total internal reflection from the inner surface. When the bottom end of the beam passes the meniscus center, the entire beam will be reflected. The reflected portion of the beam progressively increases with the beam advancement and the resulting signal broadening will then be comparable to the dimension of the beam diameter.

The beam diameter at the center of the meniscus will be equal to the pinhole diameter multiplied by the magnification of the collimating lens in the absence of diffraction (Fig. 2). However, the inevitable light diffraction enlarges the image diameter of the pinhole by a factor beyond the collimating lens magnification. Assuming that a point-spread function describes a small particle image, which is analogous to the diffraction pattern of a point source of light, the characteristic diameter of a point-spread function d_s (Born and Wolf 1980) is given as,

$$d_s = 1.22(1+M)\lambda \cdot NA^{-1} \tag{2}$$

where M is the collimating lens magnification, and λ is the wavelength of the illuminating light. The numerical aperture (NA) is defined as

$$NA \equiv n \cdot \sin\theta_{\max} \approx n_{\text{air}} \frac{r_{\max}}{L} = 0.0333 \tag{3}$$

where the object distance $L=2f=240$ mm for $M=1.0$, $\theta_{\max}$ is the maximum beam divergence of the helium–neon laser emitted from the pinhole, $n_{\text{air}}=1$, and the diverging beam radius projected on the lens surface $r_{\max}$ is measured as 8 mm.

The effective image of a point object (the pinhole) is known to be the convolution of the diffraction-limited image with the geometric image (Adrian 1997). Assuming the geometric and diffraction-limited images as Gaussian functions, an effective image diameter d_e is given as

$$\begin{aligned} d_e &= \left[M^2 d_{\text{PH}}^2 + d_s^2\right]^{1/2} \\ &= \left[M^2 d_{\text{PH}}^2 + \left\{1.22(1+M)\lambda NA^{-1}\right\}^2\right]^{1/2} = 52.6\,\mu\text{m} \end{aligned} \tag{4}$$

where the lens magnification $M=1.0$, the pinhole diameter $d_{\text{PH}}=25$ μm, $\lambda=0.6328$ μm for helium–neon laser, and $NA=0.0333$ from Eq. (3).

While the collimated laser-beam diameter is estimated to be 52.6 μm, the signal broadening is measured to be 60 μm and 70 μm for on-axis and off-axis detection, respectively, as shown for the 1.0-mm wide channel in Figs. 3a and b. The tested fluid was isopropyl-alcohol at room temperature and ambient pressure. The broadening is 14% and 33%, respectively larger than the estimated beam diameter, which may be attributed to additional broadening contributions from the aforementioned other factors. Nevertheless, the finite laser-beam diameter is shown to be the primary reason for the signal broadening.

The uncollimated laser beam of 1.1 mm diameter showed a dramatic increase in the broadening as seen in Figs. 3c and d. The radius of curvature of the meniscus is comparable to the channel half-width of 0.5 mm and the beam diameter is more than twice as large. The on-axis detection signal (Fig. 3c) is broadened to 710 μm, and thereafter, the detected intensity rises as the excessive beam portion that has already passed the curved meniscus region is transmitted through the glass channel walls to the detector. The off-axis detection (Fig. 3d) progressively increases to the maximum when the beam center reaches the meniscus bottom point and then decreases to zero showing the signal broadening to 1.63 mm. The signal broadening of the uncollimated beam is exceedingly large and the resulting uncertainties in identifying the meniscus location are unacceptably high.

3.2
Effect of capillary pore dimension

Figures 4 and 5, respectively, show on-axis and off-axis detected intensities for three different pores of 0.5, 1, and 2 mm diameters. Corresponding amounts of broadening are estimated to be 70, 70, and 75 μm for on-axis, and 100, 90, and 95 μm for off-axis detection. The dependence of the signal broadening on the pore diameter is not apparent for the tested range.

Geometric ray propagation has been considered to examine the effect of laser-beam refraction through the outer and inner interfaces of the pore, i.e., the so-called lens effect. The relatively thick pore wall can substantially refract the incident laser beam and subsequently alter the beam diameter as well as its incident angle. The analytical ray tracing technique (Hecht 2002) allows comprehensive matrix expressions that calculate the resulting ray trace from an arbitrary incident ray passing through the two circular refracting surfaces of the capillary pore wall (Fig. 6):

$$r_{t2} = \Re_2 \Im_{21} \Re_1 \cdot r_{i1} \tag{5}$$

where the ray vectors r_{t2}, r_{il}, specify the ray skew angle α and its incident location y, and they are defined as

$$r_{t2} \equiv \begin{bmatrix} n_{t2}\alpha_{t2} \\ y_{t2} \end{bmatrix}, \qquad r_{i1} \equiv \begin{bmatrix} n_{i1}\alpha_{i1} \\ y_{i1} \end{bmatrix} \tag{6}$$

and the refraction matrices are defined at the inner and outer surface, respectively, as

$$\Re_2 \equiv \begin{bmatrix} 1 & -\frac{(n_{t2}-n_{i2})}{R_2} \\ 0 & 1 \end{bmatrix}, \qquad \Re_1 \equiv \begin{bmatrix} 1 & -\frac{(n_{t1}-n_{i1})}{R_1} \\ 0 & 1 \end{bmatrix}. \tag{7}$$

The transfer matrix describes the ray transmission through the pore wall thickness, which is defined as,

$$\Im_{21} \equiv \begin{bmatrix} 1 & 0 \\ d_{21}/n_{t1} & 1 \end{bmatrix} \tag{8}$$

Note that the ray skew angle, α, is considered to be positive when measured clockwise from the horizon for both incident and transmitted rays (thus all four angles of α in Fig. 6 are positive), and the paraxial ray tracing assumes that $d_{21} \approx R_1 - R_2$. Indeed, the paraxial ray assumption is valid since the collimated laser beam of small diameter is incident on the center of the relatively large pore surface ($y \ll R_1$ or R_2) nearly in parallel to the optical axis ($\alpha \approx 0$).

Using $n_{i1}=n_0$, $n_{t1}=n_{i2}=n_g$, $n_{t2}=n_l$, $\alpha_{il}=\alpha_o$, $\alpha_{t2}=\alpha$, $y_{il}=y_o$, $y_{t2}=y$, $R_1=R$, and $R_2=\chi R_1=\chi R$, with χ being the ratio of the inner diameter to the outer diameter of the pore, substitution of Eqs. (6), (7), and (8) into Eq. (5) is given as,

$$\begin{bmatrix} n_l\alpha \\ y \end{bmatrix} = \begin{bmatrix} 1+\frac{1-\chi}{\chi}\frac{n_g-n_l}{n_g} & -\frac{n_g-n_o}{R}+\frac{n_g-n_l}{\chi R}-\frac{(n_g-n_l)(n_g-n_o)}{n_g R}\frac{1-\chi}{\chi} \\ \frac{(1-\chi)R}{n_g} & 1-(1-\chi)\frac{n_g-n_o}{n_g} \end{bmatrix} \begin{bmatrix} n_o\alpha_o \\ y_o \end{bmatrix} \tag{9}$$

where the subscripts o, g, and l denote air, glass pore wall, and working fluid inside the pore, respectively. The paraxial assumption of $\alpha_o \approx 0$ and $y_o \ll R$ allows the combined implicit solutions for α and y of the matrix Eq. (9) to be uncoupled to individual explicit solutions as:

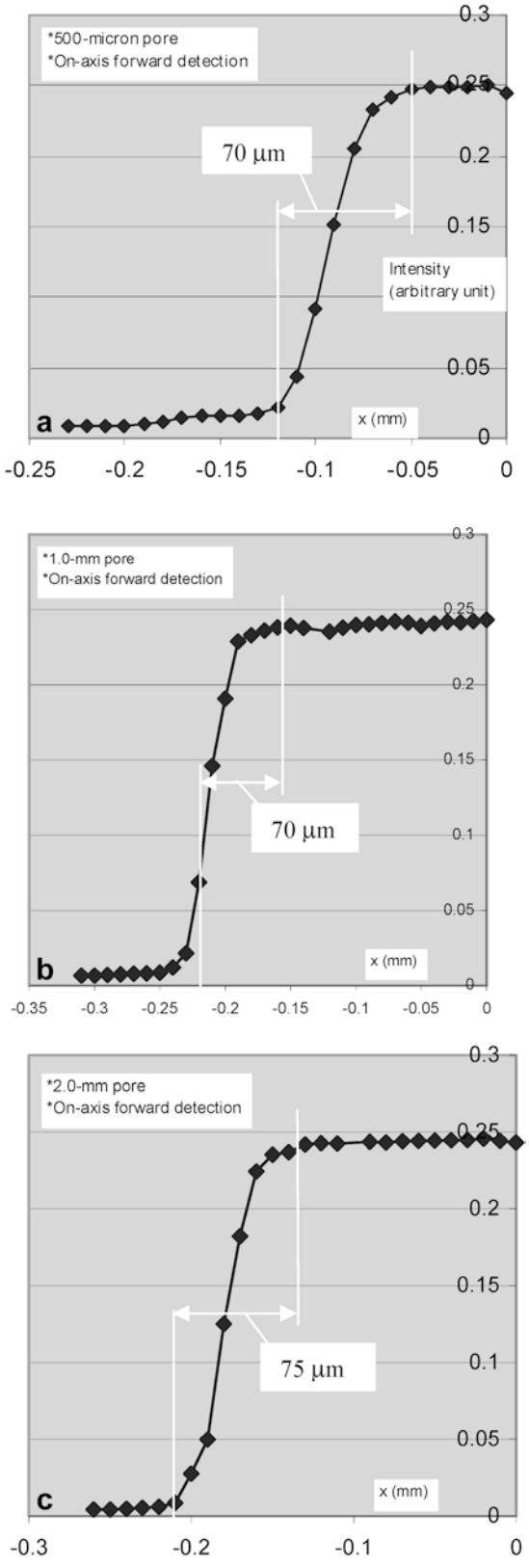

Fig. 4a–c. Signal broadening of on-axis recorded image intensity. **a** 70 µm (0.5 mm pore), **b** 70 µm (1.0 mm pore), and **c** 75 µm for (2.0 mm pore)

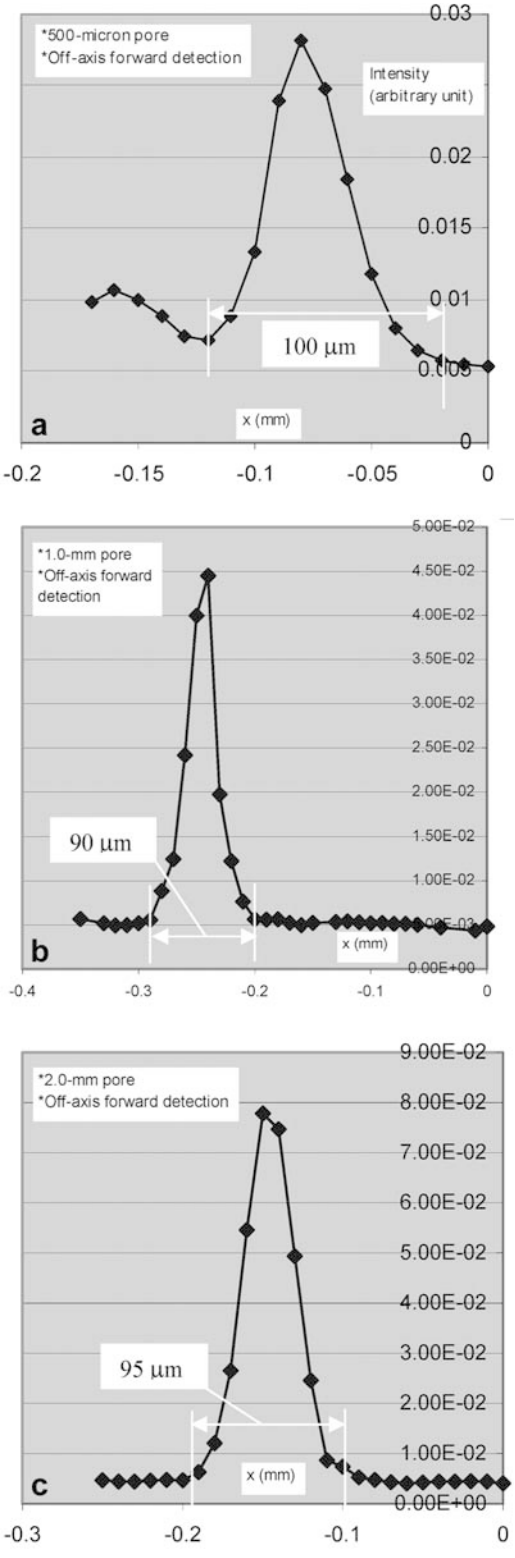

Fig. 5a–c. Signal broadening for off-axis recorded image intensity. **a** 100 µm (0.5 mm pore), **b** 90 µm (1.0 mm pore), and **c** 95 µm (2.0 mm pore)

$$\text{for } \alpha_o \approx 0: \quad \frac{y}{y_o} \sim \left[1 - (1-\chi)\cdot\frac{n_g - n_o}{n_g}\right] \tag{10}$$

$$\text{for } y_o \approx 0: \quad \frac{\alpha}{\alpha_o} \sim \frac{n_o}{n_l}\left[1 + \frac{1-\chi}{\chi}\cdot\frac{n_g - n_l}{n_g}\right] \tag{11}$$

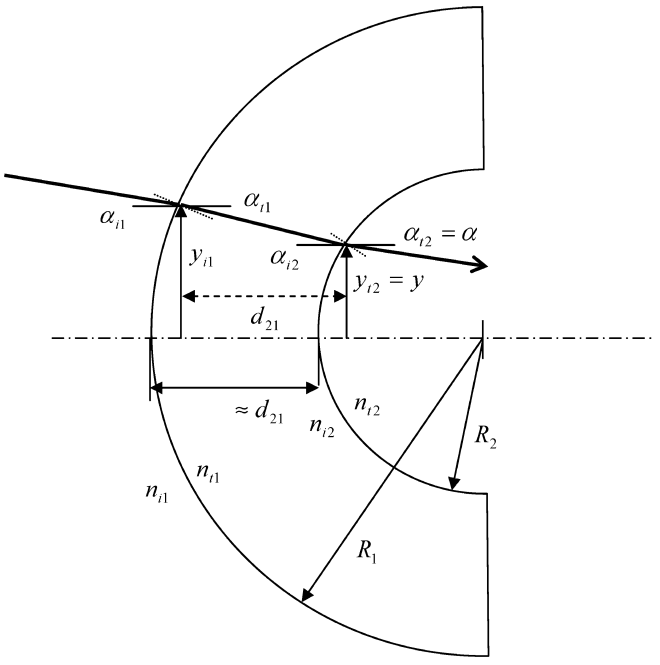

Fig. 6. Schematic illustration of ray geometry through the capillary pore wall

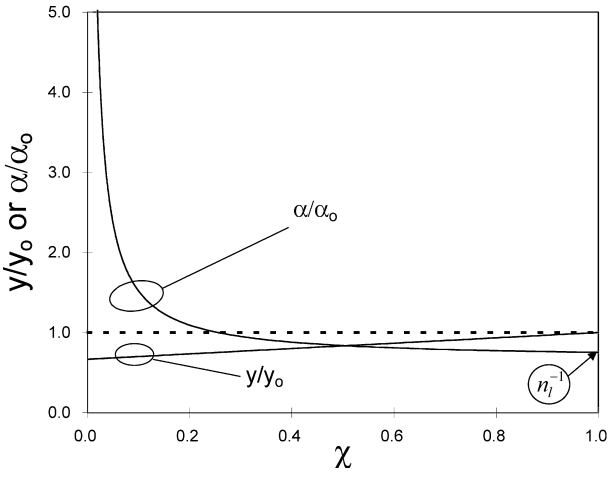

Fig. 7. Analytical ray tracing calculation results of y/y_o (Eq. 10) and α/α_0 (Eq. 11) vs. the pore inner to outer diameter ratio, χ (n_o=1.0, n_l=1.33 and n_g=1.5)

Figure. 7 shows y/y_o and α/α_o versus χ ranging from 0 to 1 for n_o=1.0, n_l=1.33 (for a typical liquid such as water) and n_g=15 (glass pore). The three tested pores have the same 5 mm outer diameter and χ=0.1, 0.2, and 0.4 for the 0.5, 1.0, and 2.0 mm inner diameter, respectively. The limiting case of χ=0 represents a solid rod of 5 mm diameter. The virtual case of χ=1 represents a pore of zero wall thickness with the only refraction occurring in the liquid inside the pore, i.e., y/y_o=1 and α/α_o=1/n. The laser-beam radius ratio y/y_o decreases from 1 linearly with a decreasing inner pore diameter or χ, which tends to reduce the beam diameter in the test meniscus region. The incident beam angle ratio α/α_o, on the other hand, increases almost linearly from $1/n_l$ to χ~0.1, which tends to enlarge the beam diameter, and then very quickly increases thereafter as χ approaches 0. These two adverse effects between y/y_o and α/α_o, particularly for the present test range of χ from 0.4 down to 0.1, counter-balance each other and favorably support the finding of no noticeable dependence of signal broadening for the 0.5, 1, and 2-mm diameter pores tested, as seen in Figs. 4 and 5.

3.3
Effect of beam steering by temperature gradient

When heat is transferred into the meniscus region, a non-isothermal condition may be established in the working fluid and the collimated laser beam can be steered to contribute additionally to the signal broadening. A primary temperature gradient is assumed to exist in the perpendicular direction (y) of the beam incidence, i.e., from the heated pore outer surface to the relatively cooler working fluid inside (Fig. 8). An axi-symmetric pore configuration neglects the azimuthal temperature gradient normal to the incident ray, and thus, the beam steering, caused by the normal component of temperature gradient, is negligible. Within the context of geometrical optics, Fermat's Principle describes the propagation of a single light ray through a medium and states that the light wave will take a path that involves the least travel time. The use of a paraxial approximation, i.e., the amount of ray diffraction in the medium being very small and the light ray remaining nearly straight, the diffraction-angle component, ε_y is expressed as the path integral along the optical axis (Weyl 1954):

$$\tan\varepsilon_y \approx \varepsilon_y = \int_{\zeta_1}^{\zeta_2} \frac{1}{n(x,y)}\frac{\partial n}{\partial y}\mathrm{d}x \cong \frac{1}{n_o}\frac{\mathrm{d}n}{\mathrm{d}y}\Delta x = \frac{1}{n_o}\frac{\mathrm{d}n}{\mathrm{d}T}\frac{\mathrm{d}T}{\mathrm{d}y}\Delta x \tag{12}$$

In the case of water (n_0=1.3331733 at T=0°C), the expression for dn/dT (Radulovic 1977) is given as,

$$\frac{\mathrm{d}n}{\mathrm{d}T} = -0.00001\,(1.936 + 2\times 0.1699T) \tag{13}$$

where T may be considered to be the mean or bulk temperature of the liquid in the pore. For water, at temperature range between 20 and 34°C, a very accurate measurement of the refractive index gives a cubic formula (Lira 1994) fitting as,

$$\frac{\mathrm{d}n}{\mathrm{d}T} = -0.00001[8.376 + 2\times 0.2644\,(T - 20^\circ\mathrm{C}) - 0.00479\times 3(T-20^\circ\mathrm{C})^2] \tag{14}$$

Figure 9 shows the calculated diffraction angle ε_y as a function of the medium temperature gradient dT/dy using Eq. (12) in conjunction with Eqs. (13) and (14), for a typical optical path length of Δx~1.0 mm, which is comparable to the capillary pore diameter. Several different values for bulk temperature T in Eqs. (13) and (14) were used for subcooling, saturated, and superheated states of water. Both predictions agree well with each other at least for the effective range of the prediction by Lira (1994), from 20 to 34°C, showing the two results virtually identical

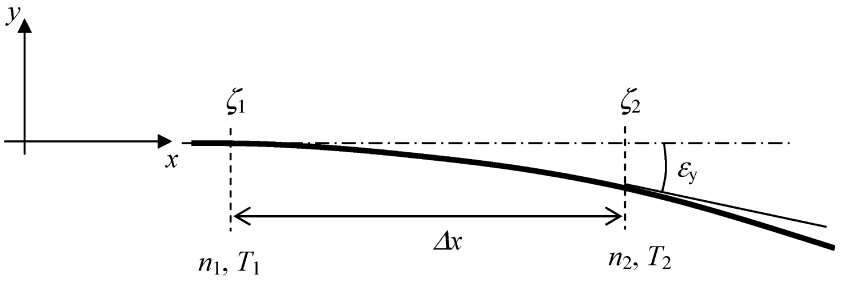

Fig. 8. A schematic illustration of beam steering by temperature gradient in the *y* direction

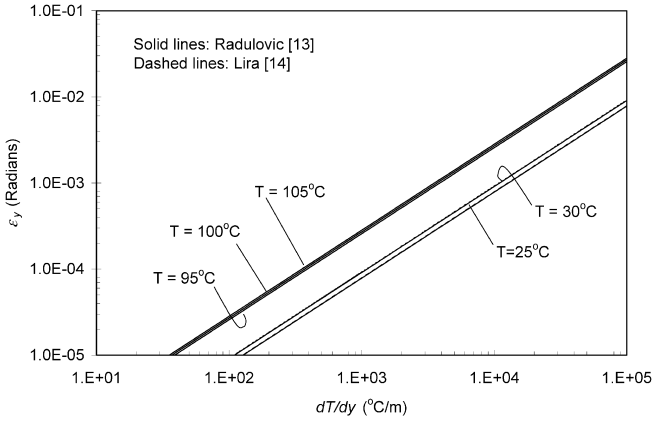

Fig. 9. Calculated diffraction angles (ε_y) as functions of the medium temperature gradient (d*T*/d*y*) based on two different predictions (Eqs. 13 and 14)

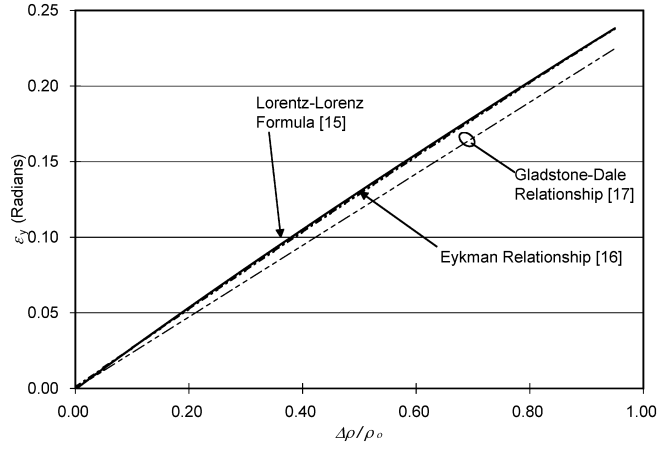

Fig. 10. Calculated diffraction angles [$\varepsilon_y \equiv \Delta n/n_o=(n_o-n)/n_o$] vs. the relative density variation [$\Delta\rho/\rho_o \equiv (\rho_o-\rho)/\rho_o$] based on three different predictions: (1) Lorentz–Lorenz formula by Eq. (15), (2) Eykman relationship by Eq. (16), and (3) Gladstone–Dale relationship by Eq. (17)

to each other. The diffraction angle linearly increases with an increasing temperature gradient, as expected from Eq. (12), and also increases, with an increasing bulk temperature, since the (absolute) magnitude of d*n*/d*T* increases with the bulk temperature both in Eqs. (13) and (14).

Using temperature gradient d*T*/d*y*=10^4°C/m as an example for an extremely high temperature gradient, available from a published capillary experiment (Pratt and Hallinan 1997), ε_y for saturated water at 100°C under 1 atm is calculated to be 2.690×10^{-3}rad (0.15°). The resulting contribution to the beam broadening is estimated by $\Delta d\approx\varepsilon_y\Delta x$=2.69 μm at the meniscus bottom where the total reflection takes place. The thermally driven diffraction can be considered small in most cases because of the generally small length scales of Δx involved with a capillary pore.

3.4
Effect of beam steering by concentration gradient

In a mixture of two different fluids refractive index varies with local density variations depending on the local mixture composition. Both analytical and empirical expressions have been formulated for refractive index as functions of medium density.

If Maxwell's relation between dielectric constant ε and refractive index n is used, i.e., $\varepsilon=n^2$, the Lorentz–Lorenz formula (Feynman et al. 1964) is derived by analytically considering the mean polarizability to give an expression for refractive index:

$$\frac{n^2-1}{n^2+2}=\frac{\rho}{M}A \tag{15}$$

where M is the molecular weight and A is called molar refractivity, for example, for water M=18 and A=3.71 cm^3/g mole at 20°C.

On the other hand, the Eykman relationship (Lading et al. 2001) was derived empirically and is known to perform better than the Lorentz–Lorenz formula:

$$\frac{n^2-1}{n+0.4}=\rho\cdot\text{const} \tag{16}$$

where the constant is calculated as 0.44721 cm^3/g for water from its reference property values of ρ_o=1.0 g/cm^3 and n_o=1.332155 at 20°C.

If the Gladstone–Dale relationship is used (Merzkirch 1987), the refractive index shows a linear increase, with increasing density, as:

$$n=1+K\rho \tag{17}$$

where the Gladstone–Dale constant K=0.310 cm^3/g for water at 273K for λ=0.6328 μm.

Assuming that $\Delta x\approx\Delta y\approx d_{pore}$, i.e., the ray path length, Δx, is comparable to the length scale for the density variation, Δy, and both length scales are on the same order of the capillary pore diameter, d_{pore}, Eq. (12) is reduced to:

$$\varepsilon_y\approx\frac{\Delta n}{n_o}\equiv\frac{|n-n_o|}{n_o} \tag{18}$$

Table 1. Magnitudes of signal broadening with a filtered and collimated laser beam of 52.6 μm diameter used, and uncertainty levels[a] for wicking height determination

Two-dimensional channel			Axi-symmetric pore		
Channel width (mm)	On-axis detection (μm)	Off-axis detection (μm)	Pore diameter (mm)	On-axis detection (μm)	Off-axis detection (μm)
0.5	60 (±3.7)	70 (±8.7)	0.5	70 (±8.7)	100 (±23.7)
1.0	60 (±3.7)	70 (±8.7)	1.0	70 (±8.7)	90 (±18.7)
2.0	65 (±6.2)	85 (±16.2)	2.0	75 (±11.2)	95 (±21.2)

[a]Uncertainty level $\equiv \pm\left[\frac{\text{Signal broadening}-52.6\,\mu\text{m}}{2}\right]$

For example, for pure water ρ_o=1.0 g/cm^3 at 20°C, n_o is either calculated or given to be 1.3337415, 1.332155, and 1.310 by Eqs. (15), (16), and (17), respectively. Using these reference values of n_o and ρ_o, different values of n for different mixture density levels of ρ are calculated using the same equations, and the resulting diffraction angles are calculated from Eq. (18). Figure. 10 shows calculated diffraction angles, $\varepsilon_y \equiv [n_o - n]/n_o$, that progressively increase with the normalized density reduction of the mixture, $[\rho_o - \rho]/\rho_o$. Both the Lorentz–Lorenz formula, Eq. (15), and the Eykman relationship, Eq. (16), show very close agreement with each other, whereas the Gladstone–Dale relationship, Eq. (17), deviates from these two predictions, with increasing mixture concentration.

As an example, a relatively large concentration variation of 10% ($\Delta\rho/\rho$=0.1), as presented in a published capillary pore experiment using a binary mixture working fluid (Pratt and Kihm 2003), the diffraction angle ε_y is calculated as 0.02683 rad (1.537°) by the Lorentz–Lorenz formula, 0.02685 rad (1.538°) by the Eykman relationship, and 0.02366 rad (1.356°) by the Gladstone–Dale relationship. Thus, the contributing magnitude to the beam broadening, $\varepsilon_y \cdot \Delta x$ with $\Delta x \approx 1.0$ mm, can be as large as 27 μm at the beam intersection location at the meniscus bottom. The magnitude of the diffraction angles, caused by the mixture density gradient, can be an order of magnitude larger than the magnitude of the thermally driven diffraction angles.

3.5 Overall measurement uncertainty

Since the detected signal is likely symmetrically broadened, determination of the wicking height can be acquired from the medium point of the detected signal, either of the gradually increasing signal for the on-axis detection, or the Gaussian shape signal for the off-axis detection. The amount of signal broadening, equal to the collimated beam diameter of 52.6 μm under diffraction, will be inherent and inevitable, and only the excessive amount of broadening beyond the estimated beam diameter will account for the overall measurement uncertainty. One-half of the excessive broadening is estimated for the uncertainty in determining the meniscus bottom location, as the maximum possible range of uncertainty.

Table 1 shows the summary of the measured magnitudes of signal broadening and estimated uncertainties for all the tested conditions. The signal broadening shows a very weak or nearly negligible increase with increasing channel or pore dimension. The off-axis detection shows larger broadening than the on-axis detection by 15–40%. The wicking height measurement uncertainties are estimated to be up to ±12 μm for the on-axis detection, and better than ±24 μm for the off-axis detection.

4 Concluding remarks

A laser-scanning technique for accurate and repeatable wicking height measurements has been devised using the principle of total internal reflection of a collimated laser beam from the meniscus formed in a capillary pore. The implemented system has been tested to examine the detected signal broadening that potentially degrades its measurement accuracy. The empirical and analytical findings on the estimated importance of these broadening factors are:

1. Effect of a finite beam diameter—the diffraction principle estimates the collimated laser-beam diameter significantly larger than the initial pinhole size, and this finite and enlarged beam diameter primarily contributes to the overall signal broadening for both on-axis and off-axis detection.
2. Effect of the capillary pore diameter—the analytical ray tracing calculation shows that adverse lens effects on the beam diameter distortion and on the ray angle distortion tend to counteract and no distinctive dependence of the signal broadening on the tested pore diameters (0.5, 1.0, and 2.0 mm inner diameter with a common 5.0 mm outer diameter).
3. Effect of thermal beam steering—the thermally-driven steering angle by non-zero liquid temperature gradient is predicted to be on the order of 10^{-3}rad or less for a typical example of saturated water up to an excessively high range of $dT/dy = 10^4$°C/m.
4. Effect of beam steering by concentration gradient—the density-driven diffraction angle, on the other hand, can be an order of magnitude larger than the thermally driven effect of (3), for example, for the case of an excessive density differential of up to 10%.
5. The wicking height measurement uncertainties for all three tested pores or channels of 0.5, 1.0, and 2.0 mm dimensions are estimated to be up to ±12 μm in the case of on-axis detection, and up to ±24 μm in the case of off-axis detection.

References

Adrian RJ (1997) Dynamic ranges of velocity and spatial resolution of particle image velocimetry. Meas Sci Technol 8:1393–1398

Anderson DM, Davis SH (1994) Local fluid and heat flow near contact lines. J Fluid Mech 268:231–265

Born M, Wolf E (1980) Principles of optics, 6th edn. Pergamon Press, Oxford, pp 84–90

Chan SH, Zhang W (1994) Rewetting theory and the dryout heat flux of smooth and grooved plates with a uniform heating. J Heat Transfer 116:173–179

Ehrhard P, Davis SH (1991) Non-isothermal spreading of liquid drops on horizontal plates. J Fluid Mech 229:365–388

Feynman RP, Leighton RB, Sands M (1964) Lectures on physics, vol II. Addison-Wesley, Reading, Mass., p 32

Ha JM, Peterson GP (1994) Analytical prediction of the axial dryout point for evaporating liquids in triangular microgrooves. J Heat Transfer 116:498–503

Hecht E (2002) Optics, 4th edn. Addison-Wesley, Reading, Mass., p 12

Hocking LM (1995) On contact angles in evaporating liquids. Phys Fluids 7:2950–2955

Lading L, Wigley G, Buchhave P (2001) Optical diagnostics for flow processes. Plenum Press, New York, pp 192–194

Lira IH (1994) Reconstruction of an axisymmetric refractive index distribution with non-negligible refraction. Meas Sci Technol 5:226–232

Merzkirch W (1987) Flow visualization, 2nd edn. Academic Press, Orlando, Fl., pp 116–123

Pratt DM, Hallinan KP (1997) Thermocapillary effects on the wetting characteristics of a heated curved meniscus. J Thermophys Heat Transfer 11:519–525

Pratt DM, Kihm KD (2003) Binary fluid mixture and thermocapillary effects on the wetting characteristics of a heated curved meniscus. J Heat Transfer (in press)

Radulovic PT (1977) Holographic interferometry of three-dimensional temperature or density fields. PhD dissertation, Department of Mechancial Engineering and Applied Mechanics, University of Michigan, Ann Arbor, Mich.

Sen AK, Davis SH (1982) Steady thermocapillary flows in two-dimensional slots. J Fluid Mech 121:163–186

Weyl FJ (1954) Analysis of optical methods. In: Ladenburg RW (ed) Physical measurements in gas dynamics and combustion. Princeton University Press, Princeton, N.J., pp 3–25